RESEARCH ARTICLE | FEBRUARY 18 2021

The dynamics of parallel-plate and cone–plate flows

Anand U. Oza ; David C. Venerus

Physics of Fluids 33, 023102 (2021)
https://doi.org/10.1063/5.0036980

Physics of Fluids ARTICLE scitation.org/journal/phf

The dynamics of parallel-plate and cone–plate flows

Cite as: Phys. Fluids **33**, 023102 (2021); doi: 10.1063/5.0036980
Submitted: 10 November 2020 · Accepted: 9 December 2020 ·
Published Online: 18 February 2021

Anand U. Oza[1] and David C. Venerus[2,a)]

AFFILIATIONS

[1]Department of Mathematical Sciences, New Jersey Institute of Technology, Newark, New Jersey 07102, USA
[2]Department of Chemical and Materials Engineering, New Jersey Institute of Technology, Newark, New Jersey 07102, USA

[a)]Author to whom correspondence should be addressed: venerus@njit.edu

ABSTRACT

Rotational rheometers are the most commonly used devices to investigate the rheological behavior of liquids in shear flows. These devices are used to measure rheological properties of both Newtonian and non-Newtonian, or complex, fluids. Two of the most widely used geometries are flow between parallel plates and flow between a cone and a plate. A time-dependent rotation of the plate or cone is often used to study the time-dependent response of the fluid. In practice, the time dependence of the flow field is ignored, that is, a steady-state velocity field is assumed to exist throughout the measurement. In this study, we examine the dynamics of the velocity field for parallel-plate and cone–plate flows of Newtonian fluids by finding analytical solutions of the Navier–Stokes equation in the creeping flow limit. The time-dependent solution for parallel-plate flow is relatively simple as it requires the velocity to have a linear dependence on radial position. Interestingly, the time-dependent solution for cone–plate flow does not allow the velocity to have a linear dependence on radial position, which it must have at the steady state. Here, we examine the time-dependent velocity fields for these two flows, and we present results showing the time dependence of the torque exerted on both the stationary and rotating fixtures. We also examine the time dependence of spatial non-homogeneities of the strain rate. Finally, we speculate on the possible implications of our results in the context of shear banding, which is often observed in parallel-plate and cone–plate flows of complex fluids.

I. INTRODUCTION

Since the 1930s, rotational rheometers have been used to investigate the rheological behavior of liquids in shear flows. Two of the most commonly used geometries are flow between parallel plates and flow between a cone and a plate.[1,2] Shear flow in the liquid is generated by rotating one of the fixtures (say, the cone) while the other (the plate) is held stationary. Rheological material functions such as viscosity and normal stress differences are determined from the torque and force exerted on a fixture. Nowadays, commercial instruments with sophisticated drive systems and torque/force transducers are widely used in both academic and industrial laboratories. These devices are used to study the rheology of Newtonian fluids (e.g., water, low-molecular weight organics) and non-Newtonian fluids (e.g., polymeric liquids, colloidal dispersions, biological matter).

For Newtonian (linearly viscous) fluids, shear stress is a linear function of the instantaneous shear rate—the two being related by a constant viscosity η. By contrast, non-Newtonian fluids, in general, exhibit a non-linear and time-dependent relationship between shear stress and shear rate, and they may also display normal stress differences. To study such fluids, the imposed shear rate is time dependent (i.e., step function, delta function, oscillatory). The response of the fluid is measured and used to extract a time-dependent viscosity, or frequency-dependent dynamic modulus, for example.[3]

The utility of parallel-plate and cone–plate flows relies on the ability to induce a *rheologically controlled* flow, that is, a flow having a single non-zero component of the velocity vector that leads to a single non-zero component of the rate of deformation (or strain) tensor, which is the shear rate. For both parallel-plate and cone–plate geometries, the shear rate and, hence, the stress are not uniform within the liquid sample. Since the torque and force on a fixture are measured at a particular surface, the spatially varying stress in these flows must be taken into account if one is interested in measuring material functions for non-Newtonian fluids. For the cone and plate geometries, the variation of shear rate can be neglected for small cone angles.[3–5]

Given the widespread use of parallel-plate and cone–plate flows, it is not surprising that significant effort has been focused on factors that may cause deviations from a rheologically controlled flow. These factors include secondary flows induced by inertia (centrifugal forces)

and/or fluid elasticity,[6–10] edge effects where the liquid is in contact with an ambient gas,[11–14] and slip between the fluid and solid fixtures.[15] Additional factors such as viscous heating[16,17] and transducer compliance[18–20] have also been considered.

A common rheological experiment is to induce flow in an initially quiescent sample by rotating the cone (or plate) at a constant angular velocity Ω. The velocity field within the sample evolves in time to a steady state that ideally is a rheologically controlled flow. The timescale for momentum diffusion is $\tau = L^2/\nu$, where L is the characteristic length of the flow field and $\nu = \eta/\rho$ is the kinematic viscosity of the fluid. Typically, $L \sim 10^{-2}$ m, and for water, $\nu \sim 10^{-6}\,\mathrm{m}^2/\mathrm{s}$ so that $\tau \sim 100$ s or smaller. For fluids with a large viscosity, the time required to reach a steady-state flow field typically is much smaller than the rheological characteristic time of the sample. It would, therefore, seem reasonable to assume that the dynamics of the flow field in rotational rheometers can safely be ignored. In fact, investigations of the flow field dynamics in rotational rheometers are practically nonexistent. One exception is an analysis of the time-dependent tangential flow of a Newtonian fluid in an annulus.[21] In addition, time-dependent cone and plate flows have been examined using numerical solutions of the governing equations; however, the paper lacked sufficient information to interpret the dynamic behavior of the velocity field.[22]

It appears that analytical solutions for transient parallel-plate and cone–plate flows, even for Newtonian fluids where the governing equations are linear, heretofore have not been obtained. In this study, we examine time-dependent flows of Newtonian fluids between parallel plates and between a cone and a plate. In particular, we obtain exact analytical solutions to these fluid mechanics problems to examine the spatiotemporal evolution of the velocity field within the sample and the dynamics of the measured torque.

II. ANALYTICAL SOLUTIONS OF FLOW PROBLEMS

We consider laminar flows of a Newtonian fluid with constant density ρ and viscosity η and neglect both inertial[6,8] and external (gravitational) forces. Hence, we find solutions to the Navier–Stokes equation in the creeping flow limit,

$$\rho\frac{\partial \boldsymbol{v}}{\partial t} = \eta\nabla^2\boldsymbol{v} - \nabla p^{\mathrm{L}}, \tag{1}$$

where the velocity field $\boldsymbol{v}$ is subject to the constraint $\nabla\cdot\boldsymbol{v} = 0$ and p^{L} is the (pseudo)pressure field.[23] We note that neglecting inertia while keeping the time-derivative in (1) follows when different characteristic times for velocity ($1/\Omega$) and time (τ) are used to put the Navier–Stokes equation in dimensionless form. For the flows considered here, we assume the velocity vector has one non-zero component in the direction of the rotating fixture. This is consistent with the assumption that inertial (centrifugal) forces can be neglected, and it ensures that the two components of the Navier–Stokes equation in the directions orthogonal to the flow direction are compatible. When the periodicity of the domain in the flow direction is also taken into account, the pseudo-pressure field is uniform: $\nabla p^{\mathrm{L}} = \boldsymbol{0}$. We further assume that the gas surrounding the liquid sample is inviscid and that interfacial stresses can be ignored.

A. Parallel-plate flow

Flow between parallel plates, sometimes called torsional flow, is shown schematically in Fig. 1. The radius of the plates is R, and they are separated by a distance H. The fluid is initially at rest, and for $t > 0$, the upper plate rotates with angular velocity Ω. The postulated velocity field is given by $v_r = v_z = 0$ and $v_\theta = v_\theta(r, z, t)$, which is compatible with the constraint on velocity for incompressible flow. The gas–liquid interface is assumed to be cylindrical so that the shear stress must vanish at $r = R$.

Compatibility of the r-component and z-component of the Navier–Stokes equation follows from the creeping flow assumption. The θ-component of the Navier–Stokes equation is given by

$$\frac{\partial v_\theta}{\partial t} = \frac{\partial}{\partial r}\left(\frac{1}{r}\frac{\partial}{\partial r}(rv_\theta)\right) + \frac{1}{\alpha}\frac{\partial^2 v_\theta}{\partial z^2}, \tag{2}$$

where we have made this equation dimensionless using $r/R \to r$, $z/H \to z$, $\nu t/R^2 \to t$, $v_\theta/\Omega R \to v_\theta$, where $\alpha = H/R$. The initial condition is

$$v_\theta(r, z, 0) = 0. \tag{3}$$

Boundary conditions on the plate surfaces are given by

$$v_\theta(r, 0, t) = 0, \qquad v_\theta(r, 1, t) = r. \tag{4}$$

Additional boundary conditions are given by

$$v_\theta(0, z, t) = 0, \qquad \frac{\partial v_\theta}{\partial r}(1, z, t) - v_\theta(1, z, t) = 0, \tag{5}$$

where the second condition follows from the requirement that the shear stress must vanish at the free surface.

The well-known steady-state solution to this problem can be written as $v_\theta(r, t, \infty) = rz$. Based on this, we introduce the variable v given by

$$v(r, z, t) = v_\theta(r, z, t) - rz. \tag{6}$$

Hence, we write (2) as

$$\frac{\partial v}{\partial t} = \frac{\partial}{\partial r}\left(\frac{1}{r}\frac{\partial}{\partial r}(rv)\right) + \frac{1}{\alpha^2}\frac{\partial^2 v}{\partial z^2}. \tag{7}$$

The initial and boundary conditions in (3)–(5) become

$$v(r, z, 0) = -rz, \tag{8}$$

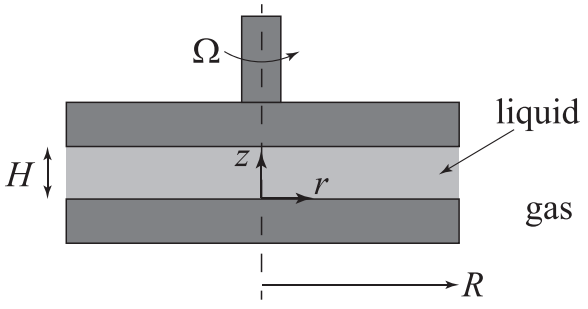

FIG. 1. Schematic of parallel-plate flow of a liquid where the lower plate is stationary and the upper plate rotates with angular velocity Ω.

$$v(r,0,t)=0, \qquad v(r,1,t)=0, \tag{9}$$

$$v(0,z,t)=0, \qquad \frac{\partial v}{\partial r}(1,z,t)-v(1,z,t)=0. \tag{10}$$

To solve (7)–(10), we use separation of variables and write $v(r,z,t)=\tilde{R}(r)Z(z)T(t)$ so that (7) becomes

$$\frac{1}{T}\frac{dT}{dt}=\frac{1}{\tilde{R}}\frac{d}{dr}\left(\frac{1}{r}\frac{d}{dr}(r\tilde{R})\right)+\frac{1}{\alpha^2 Z}\frac{d^2Z}{dz^2}. \tag{11}$$

Solving the differential equation for $\tilde{R}(r)$ and applying the boundary conditions in (10), we find

$$2J_1(\beta_m)-\beta_m J_0(\beta_m)=\beta_m J_2(\beta_m)=0, \tag{12}$$

where J_i are Bessel functions of the first kind of order i and β_m are the roots of (12). Application of the initial condition in (8) leads to

$$\int_0^1 J_1(\beta_m r)r^2 dr=\frac{J_2(\beta_m)}{\beta_m}. \tag{13}$$

From (12) and (13), we see that the solution of (7)–(10) for time-dependent parallel-plate flow excludes $v(r, z, t)$ from having a nonlinear dependence on r. In other words, surfaces at different axial locations z undergo rigid rotation about the z-axis for all times. Based on this, we try the solution

$$v(r,z,t)=rw(z,t), \tag{14}$$

which clearly satisfies (10). Equations (7)–(9) now become

$$\frac{\partial w}{\partial t}=\frac{1}{\alpha^2}\frac{\partial^2 w}{\partial z^2}, \tag{15}$$

$$w(z,0)=-z, \tag{16}$$

$$w(0,t)=0, \qquad w(1,t)=0. \tag{17}$$

Combining the solution[24] of (15)–(17) with (6) and (14) gives

$$v_\theta(r,z,t)=r\left[z-2\sum_{n=1}^{\infty}\frac{(-1)^{n-1}}{n\pi}\sin(n\pi z)\exp\left(-\frac{n^2\pi^2}{\alpha^2}t\right)\right]. \tag{18}$$

B. Cone–plate flow

We now consider flow between a stationary plate and a rotating cone, as shown schematically in Fig. 2. The radius of the plate is R, and the cone surface makes an angle β to the plate. The fluid is initially at rest, and for $t>0$, the cone rotates with angular velocity Ω. The postulated velocity field is given by $v_r=v_\theta=0$ and $v_\phi=v_\phi(r,\theta,t)$, which is compatible with the constraint on velocity for incompressible flow. The gas–liquid interface is assumed to be spherical so that the shear stress must vanish at $r=R$.

Compatibility of the r-component and θ-component of the Navier–Stokes equation follows from the creeping flow assumption. The ϕ-component of the Navier–Stokes equation takes the form

$$\frac{\partial v_\phi}{\partial t}=\frac{1}{r^2}\frac{\partial}{\partial r}\left(r^2\frac{\partial v_\phi}{\partial r}\right)+\frac{1}{r^2\sin\theta}\frac{\partial}{\partial\theta}\left(\sin\theta\frac{\partial v_\phi}{\partial\theta}\right)-\frac{v_\phi}{r^2\sin^2\theta}, \tag{19}$$

where we have used $r/R\to r$, $\nu t/R^2\to t$, $v_\phi/\Omega R\to v_\phi$ to make the equation dimensionless. The initial condition is

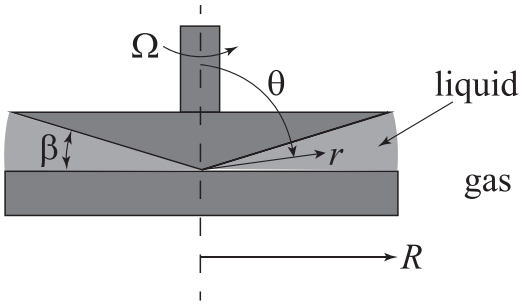

FIG. 2. Schematic of cone–plate flow of a liquid where the plate is stationary and the cone rotates with angular velocity Ω.

$$v_\phi(r,\theta,0)=0. \tag{20}$$

Boundary conditions on the plate and cone surfaces are given by

$$v_\phi(r,\pi/2,t)=0, \qquad v_\phi(r,\pi/2-\beta,t)=r\sin(\pi/2-\beta). \tag{21}$$

Additional boundary conditions are given by

$$v_\phi(0,\theta,t)=0, \qquad \frac{\partial v_\phi}{\partial r}(1,\theta,t)-v_\phi(1,\theta,t)=0, \tag{22}$$

where the second condition follows from the requirement that the shear stress must vanish at the free surface.

Based on the second boundary condition in (21), we consider a solution having the form

$$v_\phi(r,\theta,t)=r\sin\theta\, u(\theta,t), \tag{23}$$

which implies that conical surfaces of the fluid undergo rigid rotation about the z-axis. Substitution of (23) in (19) leads to

$$\frac{\partial u}{\partial t}=\frac{1}{r^2\sin\theta}\left(3\cos\theta\frac{\partial u}{\partial\theta}+\sin\theta\frac{\partial^2 u}{\partial\theta^2}\right), \tag{24}$$

which shows that a time-dependent solution of (19) does not allow v_ϕ to have a linear dependence on r as given by (23). The steady-state form of (24) is given by

$$\frac{d^2u}{d\theta^2}+3\cot\theta\frac{du}{d\theta}=0. \tag{25}$$

By integrating this equation subject to boundary conditions obtained from (21) and (23): $u(\pi/2)=0$ and $u(\pi/2-\beta)=1$, we obtain

$$u=\frac{1}{\sin\theta}\frac{\sin(\pi/2-\beta)\left[\cot\theta+\sin\theta\ln\left(\cot\frac{\theta}{2}\right)\right]}{\cot(\pi/2-\beta)+\sin(\pi/2-\beta)\ln\left[\cot\left(\frac{\pi/2-\beta}{2}\right)\right]}. \tag{26}$$

Substitution of (26) in (23) gives

$$v_\phi(r,\theta,\infty)=\frac{r\sin(\pi/2-\beta)\left[\cot\theta+\sin\theta\ln\left(\cot\frac{\theta}{2}\right)\right]}{\cot(\pi/2-\beta)+\sin(\pi/2-\beta)\ln\left[\cot\left(\frac{\pi/2-\beta}{2}\right)\right]}, \tag{27}$$

which is the steady-state solution for cone–plate flow.[5,25]

To facilitate solution of the time-dependent problem, we introduce the variable v given by

$$v(r,\theta,t) = v_\phi(r,\theta,t) - v_\phi(r,\theta,\infty), \tag{28}$$

which is governed by

$$\frac{\partial v}{\partial t} = \frac{1}{r^2}\frac{\partial}{\partial r}\left(r^2\frac{\partial v}{\partial r}\right) + \frac{1}{r^2\sin\theta}\frac{\partial}{\partial\theta}\left(\sin\theta\frac{\partial v}{\partial\theta}\right) - \frac{v}{r^2\sin^2\theta}. \tag{29}$$

From (20) and (28), the initial condition becomes

$$v(r,\theta,0) = -v_\phi(r,\theta,\infty), \tag{30}$$

and the boundary conditions are given by

$$v(r,\pi/2,t) = 0, \qquad v(r,\pi/2-\beta,t) = 0, \tag{31}$$

$$v(0,\theta,t) = 0, \qquad \frac{\partial v}{\partial r}(1,\theta,t) - v(1,\theta,t) = 0. \tag{32}$$

We proceed by introducing the change in variable

$$\xi = \cos\theta, \tag{33}$$

which transforms (29) to

$$\frac{\partial v}{\partial t} = \frac{1}{r^2}\frac{\partial}{\partial r}\left(r^2\frac{\partial v}{\partial r}\right) + \frac{1}{r^2}\frac{\partial}{\partial\xi}\left[(1-\xi^2)\frac{\partial v}{\partial\xi}\right] - \frac{v}{r^2(1-\xi^2)}. \tag{34}$$

To solve (34), we use separation of variables and write $v(r,\xi,t) = \tilde{R}(r)X(\xi)T(t)$ so that (34) becomes

$$\frac{1}{T}\frac{dT}{dt} = \frac{1}{r^2}\left\{\frac{1}{\tilde{R}}\frac{d}{dr}\left(r^2\frac{d\tilde{R}}{dr}\right) + \frac{1}{X}\frac{d}{d\xi}\left[(1-\xi^2)\frac{dX}{d\xi}\right] - \frac{1}{1-\xi^2}\right\}. \tag{35}$$

Differentiation of (35) with respect to t yields

$$\frac{1}{T}\frac{dT}{dt} = -\lambda^2, \tag{36}$$

so that (35) can be written as

$$\frac{1}{\tilde{R}}\frac{d}{dr}\left(r^2\frac{d\tilde{R}}{dr}\right) + \lambda^2 r^2 = -\frac{1}{X}\frac{d}{d\xi}\left[(1-\xi^2)\frac{dX}{d\xi}\right] + \frac{1}{1-\xi^2}. \tag{37}$$

Differentiation of (37) with respect to r yields

$$\frac{1}{\tilde{R}}\frac{d}{dr}\left(r^2\frac{d\tilde{R}}{dr}\right) + \lambda^2 r^2 = \kappa. \tag{38}$$

In the limit $r \to 0$, the solutions to (38) may be approximated by the solutions to the equidimensional equation $(r^2\tilde{R}')' - \kappa\tilde{R} = 0$. It follows that $\tilde{R} \sim r^q$ as $r \to 0$, where $q = (-1 \pm \sqrt{1+4\kappa})/2$. We, thus, conclude that $\kappa \geq 0$ in order for (38) to have a solution that is well-behaved at the origin.

Writing $\kappa = \mu(\mu+1)$, where $\mu > 0$ without loss of generality, (37) can be written as

$$\frac{1-\xi^2}{X}\frac{d}{d\xi}\left[(1-\xi^2)\frac{dX}{d\xi}\right] + \mu(\mu+1)(1-\xi^2) = 1. \tag{39}$$

The result is a pair of Sturm–Liouville eigenvalue problems,

$$\left[(1-\xi^2)X'\right]' + \left(\mu(\mu+1) - \frac{1}{1-\xi^2}\right)X = 0, \tag{40}$$

$$X(0) = 0, \quad X(\xi_0) = 0,$$

$$\left(r^2\tilde{R}'\right)' + \left[\lambda^2 r^2 - \mu(\mu+1)\right]\tilde{R} = 0,$$

$$\tilde{R}(0) = 0, \quad \tilde{R}'(1) = \tilde{R}(1), \tag{41}$$

where the primes denote differentiation with respect to the appropriate variable (r or ξ) and $\xi_0 = \cos(\pi/2-\beta)$.

First, we solve the angular equation (40), which is the associated Legendre differential equation.[26] The solution can be written as a linear combination of associated Legendre functions of the first (P_μ^1) and the second (Q_μ^1) kind of order one,

$$X(\xi) = A_\mu P_\mu^1(\xi) + B_\mu Q_\mu^1(\xi). \tag{42}$$

The boundary conditions in (40) imply that

$$A_\mu P_\mu^1(0) + B_\mu Q_\mu^1(0) = 0, \quad A_\mu P_\mu^1(\xi_0) + B_\mu Q_\mu^1(\xi_0) = 0. \tag{43}$$

These equations have a nontrivial solution if

$$f(\mu;\xi_0) \equiv P_\mu^1(\xi_0)Q_\mu^1(0) - Q_\mu^1(\xi_0)P_\mu^1(0) = 0. \tag{44}$$

The nonzero roots of $f(\mu;\xi_0)$, thus, define the eigenvalues $\{\mu_k\}_{k=1}^\infty$, where $0 < \mu_1 < \mu_2 < \cdots$, as shown in Fig. 15 in the Appendix. Note that the root $\mu = 0$ can be discarded; indeed, $P_0^1(\xi) = 0$, and $Q_0^1(0) \neq Q_0^1(\xi_0)$ for any $\xi_0 \neq 0$, so the only solution to (43) [and, thus, (40)] for $\mu = 0$ corresponds to the trivial solution $X = 0$. The eigenfunctions of (40) are, thus,

$$X_k(\xi) = P_{\mu_k}^1(\xi)Q_{\mu_k}^1(0) - Q_{\mu_k}^1(\xi)P_{\mu_k}^1(0). \tag{45}$$

We now turn to the radial equation (41), which we recognize as the spherical Bessel differential equation[27] with solution

$$\tilde{R}(r) = C_\mu j_\mu(\lambda r) + D_\mu y_\mu(\lambda r), \tag{46}$$

where j_μ and y_μ are the spherical Bessel functions of the first and the second kind,[28] respectively.

The constants in (46) are determined by satisfying the boundary conditions in (41). We note that $y_\mu(z) \to \infty$ as $z \to 0$, so $D_\mu = 0$. Since $j_\mu(0) = 0$ for $\mu > 0$, the first boundary condition in (41) is automatically satisfied. The second boundary condition gives

$$g(\lambda;\mu) \equiv \lambda j_\mu'(\lambda) - j_\mu(\lambda) = 0, \tag{47}$$

where

$$j_\mu'(r) = \frac{1}{2}\left(j_{\mu-1}(r) - j_{\mu+1}(r) - \frac{j_\mu(r)}{r}\right). \tag{48}$$

The nonzero roots of $g(\lambda;\mu_k)$, thus, define the eigenvalues $\{\lambda_{kn}\}_{n=1}^\infty$, where $0 < \lambda_{k1} < \lambda_{k2} < \cdots$, as shown in Fig. 16 in the Appendix. Note that the root $\lambda = 0$ can be discarded, since $j_\mu(0) = 0$ for $\mu > 0$. The eigenfunctions of (41) are, thus,

$$\tilde{R}_{kn}(r) = C_{\mu_k} j_{\mu_k}(\lambda_{kn} r). \tag{49}$$

The solution to the problem specified by (29)–(32) can be written as

$$v(r,\xi,t)=\sum_{n=1}^{\infty}\sum_{k=1}^{\infty}A_{kn}\left[P^1_{\mu_k}(\xi)Q^1_{\mu_k}(0)-Q^1_{\mu_k}(\xi)P^1_{\mu_k}(0)\right]\times j_{\mu_k}(\lambda_{kn}r)e^{-\lambda^2_{kn}t}. \tag{50}$$

The coefficients A_{kn} may be found by using the property that eigenfunctions of a Sturm–Liouville problem are orthogonal,

$$\int_0^{\xi_0}X_k(\xi)X_l(\xi)\,d\xi=M_k\delta_{kl},\qquad \int_0^1 r^2\tilde{R}_m(r;\mu_k)\tilde{R}_n(r;\mu_k)\,dr=N_m(\mu_k)\delta_{mn}. \tag{51}$$

From (30), we can write

$$v(r,\theta,0)=-v_\phi(r,\theta,\infty)\equiv\gamma r h(\xi), \tag{52}$$

where

$$h(\xi)=\frac{\xi}{\sqrt{1-\xi^2}}+\sqrt{1-\xi^2}\log\left(\frac{1+\xi}{\sqrt{1-\xi^2}}\right)=2\xi+O(\xi^3), \tag{53}$$

$$\gamma=-\frac{\sin(\pi/2-\beta)}{\cot(\pi/2-\beta)+\sin(\pi/2-\beta)\log\left[\cot\left(\frac{\pi/2-\beta}{2}\right)\right]}=-\frac{1}{2\beta}[1+O(\beta^2)]. \tag{54}$$

Evaluating (50) at $t=0$, multiplying both sides by $X_k(\xi)j_{\mu_k}(\lambda_{kn}r)r^2$, and integrating over the domain $0\le r\le 1, 0\le\xi\le\xi_0$, we obtain

$$A_{kn}=\gamma\frac{\int_0^1 r^3 j_{\mu_k}(\lambda_{kn}r)\,dr}{N_n(\mu_k)}\times\frac{\int_0^{\xi_0}\left[P^1_{\mu_k}(\xi)Q^1_{\mu_k}(0)-Q^1_{\mu_k}(\xi)P^1_{\mu_k}(0)\right]h(\xi)\,d\xi}{M_k}, \tag{55}$$

where

$$N_n(\mu_k)=\int_0^1 r^2 j^2_{\mu_k}(\lambda_{kn}r)\,dr \tag{56}$$

and

$$M_k=\int_0^{\xi_0}\left[P^1_{\mu_k}(\xi)Q^1_{\mu_k}(0)-Q^1_{\mu_k}(\xi)P^1_{\mu_k}(0)\right]^2 d\xi. \tag{57}$$

The complete solution to the problem specified by (19)–(22) is, thus,

$$v_\phi(r,\xi,t)=-\gamma r\left[\frac{\xi}{\sqrt{1-\xi^2}}+\sqrt{1-\xi^2}\log\left(\frac{1+\xi}{\sqrt{1-\xi^2}}\right)\right]+\sum_{n=1}^{\infty}\sum_{k=1}^{\infty}A_{kn}\left[P^1_{\mu_k}(\xi)Q^1_{\mu_k}(0)-Q^1_{\mu_k}(\xi)P^1_{\mu_k}(0)\right]\times j_{\mu_k}(\lambda_{kn}r)e^{-\lambda^2_{kn}t}, \tag{58}$$

where γ is given by (54). Details of the numerical evaluation of (58) are given in the Appendix.

III. RESULTS AND DISCUSSION

In this section, we begin with a presentation of the spatio-temporal evolution of the velocity fields for parallel-plate and cone–plate flows. Results are presented for parameter values encountered in typical rotational rheometers: $\alpha=H/R=0.05, 0.10, 0.15$ for the relative plate separation in the parallel-plate geometry and $\beta=0.05, 0.10, 0.15$ for the cone angle in the cone–plate geometry. This is followed by a presentation of the time evolution of the torques exerted by the fluid on the stationary and rotating fixtures. We also examine the spatial dependence of the rate of strain tensor during the transient period of parallel-plate and cone–plate flows.

A. Velocity fields

As discussed previously, the velocity for parallel-plate flow is linear in the radial position, meaning, for a given axial location, that the fluid undergoes rigid rotation. The rate of strain tensor $\dot{\gamma}=\nabla v+(\nabla v)^T$ for parallel-plate flow takes the form

$$[\dot{\gamma}]=\begin{bmatrix}0&0&0\\0&0&\frac{\partial v_\theta}{\partial z}\\0&\frac{\partial v_\theta}{\partial z}&0\end{bmatrix}=\begin{bmatrix}0&0&0\\0&0&r\frac{\partial w}{\partial z}\\0&r\frac{\partial w}{\partial z}&0\end{bmatrix}, \tag{59}$$

where v_θ is given by (18), and it is evident that momentum diffusion in the r-direction is absent. The evolution of the orbital angular velocity v_θ/r vs axial position for parallel-plate flow is shown in Fig. 3. From Fig. 3, we observe that the flow exhibits classical one-dimensional diffusive behavior, and from (18), we identify the characteristic timescale $\alpha^2R^2/\nu=H^2/\nu$. Increasing (decreasing) the relative plate separation α has the effect of increasing (decreasing) the timescale for diffusion.

In contrast to parallel-plate flow, a linear dependence of the velocity on radial position for cone–plate flow is only allowed at the steady state as given by (27). The dynamics of the orbital angular velocity v_ϕ/r vs polar angle for cone–plate flow is shown in Figs. 4 and 5 for two radial positions. The rate of strain tensor has a non-zero $\theta\phi$

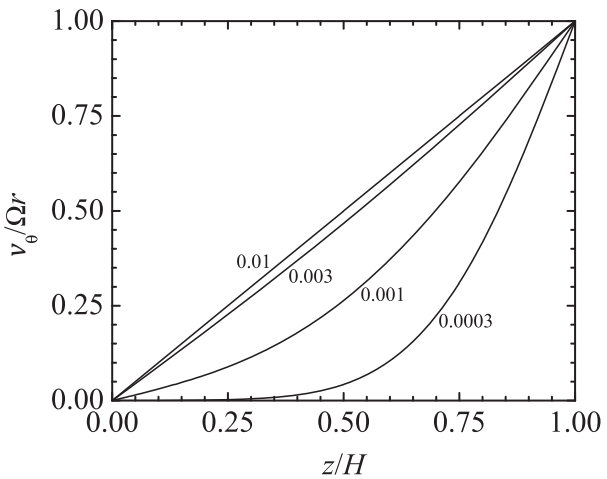

FIG. 3. Orbital angular velocity vs axial position z/H for parallel-plate flow from (18) with $\alpha=0.1$. The different curves are labeled by different times $\nu t/R^2$.

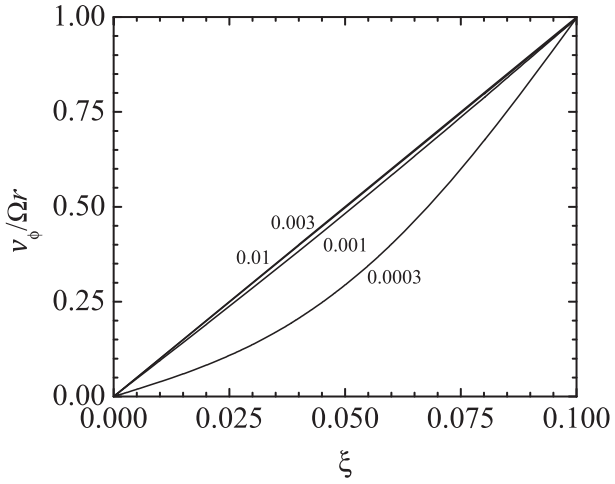

FIG. 4. Orbital angular velocity vs polar angle $\xi = \cos\theta$ for cone–plate flow from (58) with $\beta = 0.1$ for radial position $r/R = 0.5$. The different curves are labeled by different times $\nu t/R^2$.

(and by symmetry $\phi\theta$) component, and momentum diffuses in the $\xi(\theta)$-direction from the cone ($\xi = \xi_0$) to the plate ($\xi = 0$). However, the time required for the velocity to reach the steady state increases with increasing radial position. The simple explanation for this is that the gap between the cone and the plate increases with increasing radial position. This more complicated behavior observed for cone and plate flows can also be seen in Fig. 6, where the orbital angular velocity v_ϕ/r is plotted vs radial position. The nonlinear dependence of v_ϕ on r clearly shown in Fig. 6 results in the diffusion of momentum in the radial direction during the transient stage of cone–plate flow. Hence, the rate of strain tensor $\dot{\gamma}$ for cone–plate flow is given by

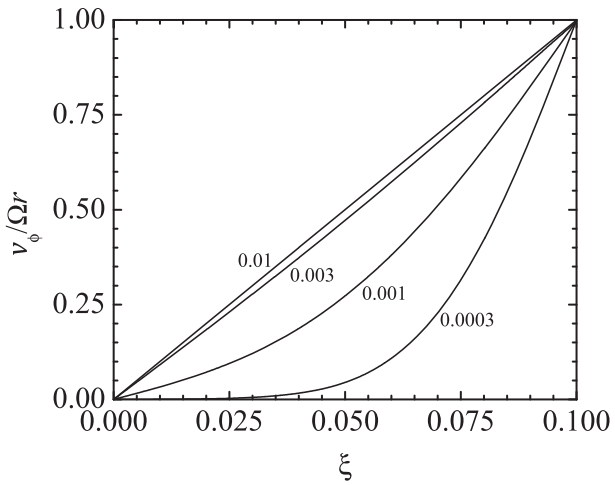

FIG. 5. Orbital angular velocity vs polar angle $\xi = \cos\theta$ for cone–plate flow from (58) with $\beta = 0.1$ for radial position $r/R = 1.0$. The different curves are labeled by different times $\nu t/R^2$.

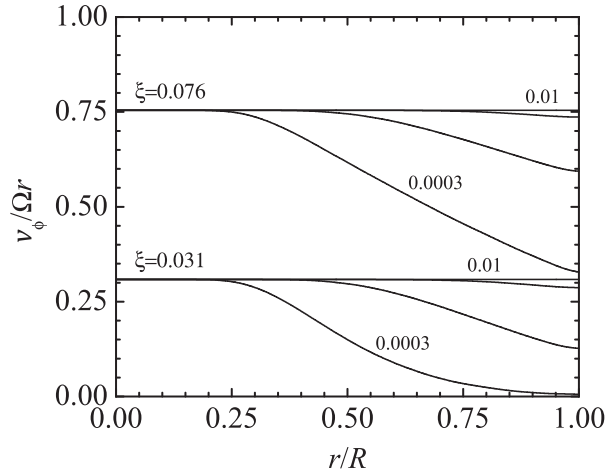

FIG. 6. Orbital angular velocity vs radial position r/R at different polar angles $\xi = \cos\theta$ for cone–plate flow from (58) with $\beta = 0.1$. The different curves are labeled by different times $\nu t/R^2 = 0.0003$, 0.001, 0.003, 0.01 (bottom to top).

$$[\dot{\gamma}] = \begin{bmatrix} 0 & 0 & r\dfrac{\partial}{\partial r}\left(\dfrac{v_\phi}{r}\right) \\ 0 & 0 & \dfrac{\sin\theta}{r}\dfrac{\partial}{\partial\theta}\left(\dfrac{v_\phi}{\sin\theta}\right) \\ r\dfrac{\partial}{\partial r}\left(\dfrac{v_\phi}{r}\right) & \dfrac{\sin\theta}{r}\dfrac{\partial}{\partial\theta}\left(\dfrac{v_\phi}{\sin\theta}\right) & 0 \end{bmatrix}. \quad (60)$$

Additional insight into the qualitative differences between parallel-plate and cone–plate flows can be garnered from the results shown in Figs. 7 and 8, which show the time evolution of the velocity fields in two spatial directions. As shown in Fig. 7 for parallel-plate flow, the velocity has a linear dependence on radial position as the velocity propagates across the gap. For cone–plate flow, we see in Fig. 8 a nonlinear dependence of velocity on radial position and the appearance of a bulge that propagates in the radial direction. A linear dependence on radial position is observed as the flow approaches the steady state for $\nu t/R^2 \geq 0.01$.

We now examine the dependence of the velocity field dynamics on the cone angle β. The dynamics of the orbital angular velocity v_ϕ/r vs polar angle is shown in Figs. 9 and 10 for cone angles $\beta = 0.05$ and $\beta = 0.15$, respectively, for radial position $r/R = 1.0$. From Figs. 4, 9, and 10, we see that the dynamics have a strong dependence on cone angle where the timescale for momentum diffusion appears to scale with β^2. Indeed, this timescale is $1/\lambda_{11}^2$, and we find that $\lambda_{11} \approx \mu_1 \approx \pi/\beta$ for small β (Fig. 17 in the Appendix).

B. Torque

In a typical parallel-plate or cone–plate experiment, the torque exerted by the fluid on the stationary or rotating fixture is used to determine the viscosity of the fluid. When the velocity field reaches the steady state, parallel-plate and cone–plate flows are in a rheologically controlled state, and the relation between the measured torque and fluid viscosity is rather simple. More importantly, this relation can be used for both Newtonian and non-Newtonian fluids. As we have

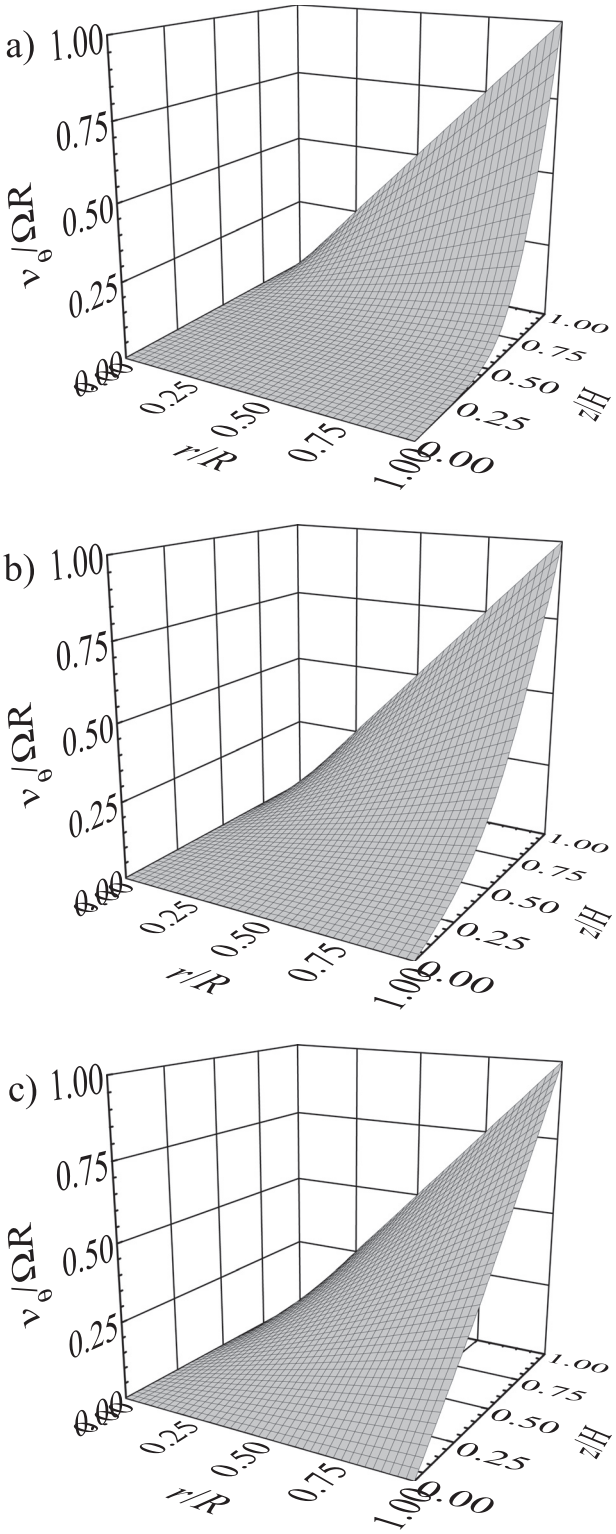

FIG. 7. Velocity vs position for parallel-plate flow from (18) with $\alpha = 0.1$ for different times $\nu t/R^2$: (a) 0.0003; (b) 0.001; (c) 0.003.

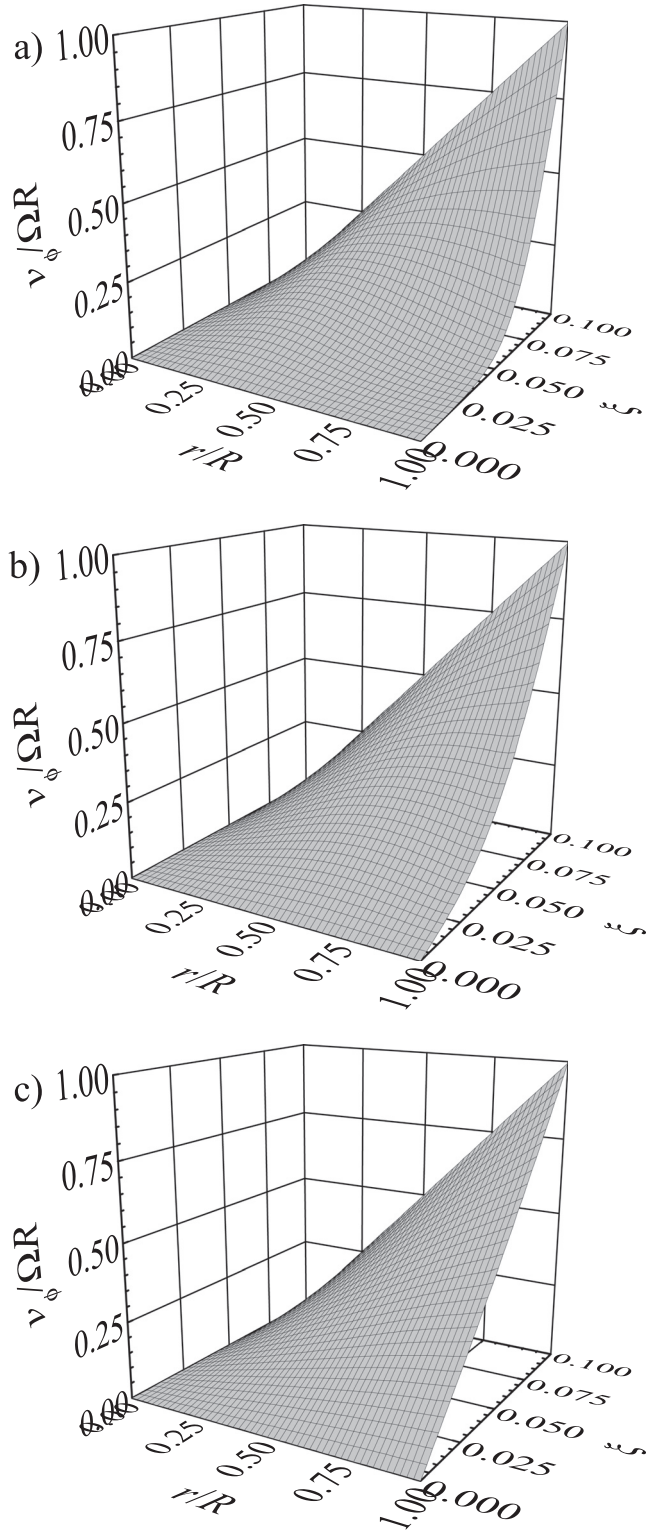

FIG. 8. Velocity vs position for cone–plate flow from (58) with $\beta = 0.1$ for different times $\nu t/R^2$: (a) 0.0003; (b) 0.001; (c) 0.003.

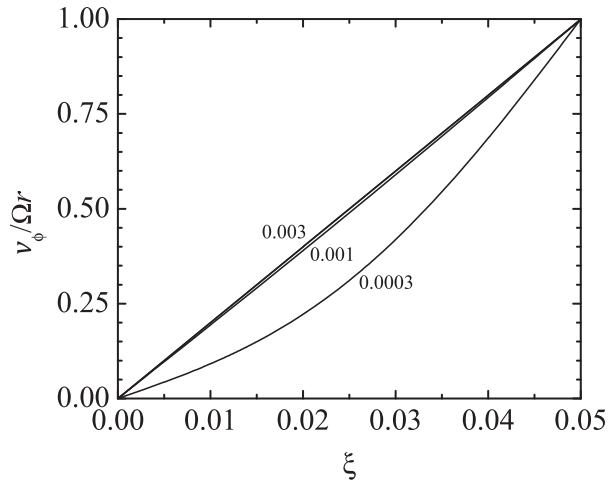

FIG. 9. Orbital angular velocity vs polar angle $\xi = \cos\theta$ for cone–plate flow from (58) with $\beta = 0.05$ for radial position $r/R = 1.0$. The different curves are labeled by different times $\nu t/R^2$.

shown, the velocity field is more complicated during the transient period. Here, we examine the time evolution of the torque for parallel-plate and cone–plate flows. The stress exerted by a fluid on a solid with unit normal vector $\boldsymbol{n}$ (pointing into the solid) is given by $\boldsymbol{n}\cdot\boldsymbol{\pi}$, where $\boldsymbol{\pi}$ is the pressure (stress) tensor. The pressure tensor can be computed from the velocity fields presented in Sec. III A.

For parallel-plate flow, the torque exerted by the liquid on the rotating or stationary plate is computed from

$$\boldsymbol{M} = \int_0^{2\pi}\int_0^R \boldsymbol{r}\times[\boldsymbol{n}\cdot\boldsymbol{\pi}]rdrd\theta, \tag{61}$$

where $\boldsymbol{r} = r\boldsymbol{\delta}_r$ and $\boldsymbol{n}\cdot\boldsymbol{\pi}$ is evaluated on the stationary ($\boldsymbol{n} = -\boldsymbol{\delta}_z$) or the rotating ($\boldsymbol{n} = \boldsymbol{\delta}_z$) plate. For Newtonian fluids, the pressure tensor takes the form $\boldsymbol{\pi} = -\eta\dot{\gamma}$, where we have set the isotropic contribution to zero and $\dot{\gamma}$ is given by (59). From the steady-state velocity: $v_\theta(r, t, \infty) = rz$, we find that the torque on the stationary plate is $M = \Omega\eta\pi R^4/2H$. Using (18) and making the torque dimensionless $M/(\Omega\eta\pi R^4/2H) \to M$, we obtain

$$\begin{aligned} M &= 1 - 2\sum_{n=1}^{\infty}(-1)^{n-1}\exp\left(-\frac{n^2\pi^2}{\alpha^2}t\right), \quad \text{stationary},\\ -M &= 1 - 2\sum_{n=1}^{\infty}(-1)^{2n-1}\exp\left(-\frac{n^2\pi^2}{\alpha^2}t\right), \quad \text{rotating}. \end{aligned} \tag{62}$$

For cone–plate flow, the torque exerted by the liquid on the cone or the plate is computed from

$$\boldsymbol{M} = \int_0^{2\pi}\int_0^R \boldsymbol{r}\times[\boldsymbol{n}\cdot\boldsymbol{\pi}]r\sin\theta drd\phi, \tag{63}$$

where $\boldsymbol{r} = r\boldsymbol{\delta}_r$ and $\boldsymbol{n}\cdot\boldsymbol{\pi}$ is evaluated on the plate ($\theta = \pi/2$, $\boldsymbol{n} = \boldsymbol{\delta}_\theta$) or the cone ($\theta = \pi/2 - \beta$, $\boldsymbol{n} = -\boldsymbol{\delta}_\theta$). Again, we set the isotropic contribution to zero so that $\boldsymbol{\pi} = -\eta\dot{\gamma}$ and $\dot{\gamma}$ is given by (60). From the steady-state solution (27), the magnitude of the torque on the plate is given by $M = -4\Omega\eta\pi R^3\gamma/3 \approx 2\Omega\eta\pi R^3/3\beta$ for $\beta \ll 1$, where γ is given by (54). Making M dimensionless using $M/(2\Omega\eta\pi R^3/3\beta) \to M$, we can write (63) as

$$\begin{aligned} M &= 1 + 3\beta\int_0^1 \frac{\partial v}{\partial\xi}(r,0,t)rdr, \quad \text{plate},\\ -M &= 1 + 3\beta(1-\xi_0^2)^{3/2}\int_0^1 \frac{\partial v}{\partial\xi}(r,\xi_0,t)rdr, \quad \text{cone}, \end{aligned} \tag{64}$$

where v is given by (50).

The time evolution of the torque M on the stationary and rotating plates for parallel-plate flow is shown in Fig. 11 for several values of the dimensionless plate separation α. The corresponding results for cone–plate flow for several values of the cone angle β are shown in Fig. 12. From these figures, we see that time required to reach a steady torque has a strong dependence on the gap between the parallel plates

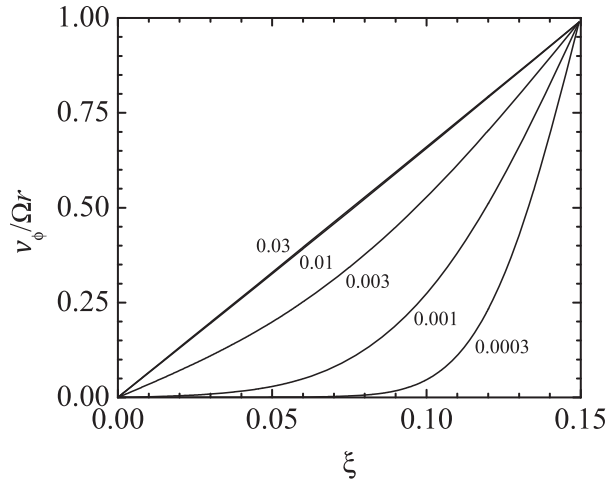

FIG. 10. Orbital angular velocity vs polar angle $\xi = \cos\theta$ for cone–plate flow from (58) with $\beta = 0.15$ for radial position $r/R = 1.0$. The different curves are labeled by different times $\nu t/R^2$.

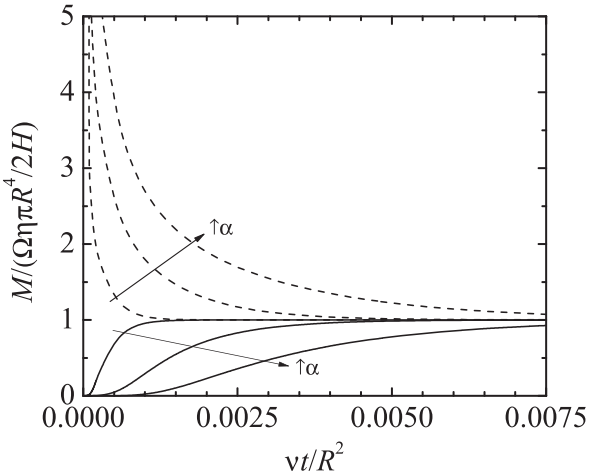

FIG. 11. Torque on stationary (solid lines) and rotating (dashed lines) plates as a function of time for parallel-plate flow from (62) with $\alpha = 0.05, 0.10, 0.15$. Note that the torque on the rotating plate is negative.

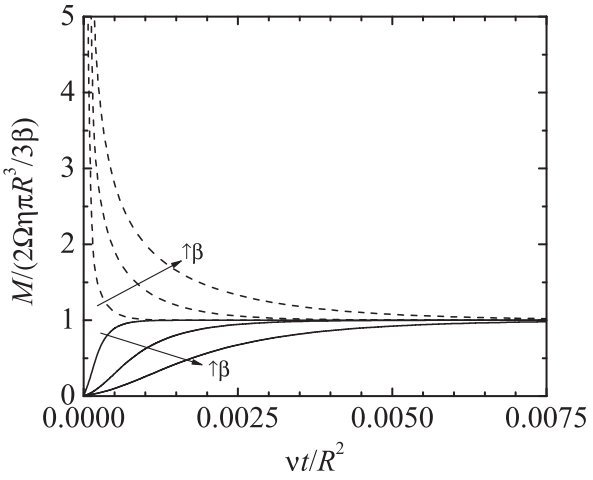

FIG. 12. Torque on plate (solid lines) and cone (dashed lines) as a function of time for cone–plate flow from (64) with $\beta = 0.05, 0.10, 0.15$. Note that the torque on the cone is negative.

α, or the cone angle β. As noted previously, the characteristic time scales with α^2 or β^2. For the largest values of these parameters considered here, the steady state is not reached until $\nu t/R^2 \gtrsim 0.01$. For liquids having a kinematic viscosity comparable to water tested in a typical geometry, the time to reach the steady state is roughly one second. It is common to use parallel-plate flow to apply sinusoidal deformations to investigate viscoelastic fluids where it is assumed that the velocity field instantaneously reaches a steady state. Based on our results, which have been obtained for Newtonian fluids, we suggest that this assumption would be valid for oscillation frequencies that are small compared to $\pi^2\nu/H^2$.

C. Rate of strain

As discussed earlier, it is a standard practice in rheometry to assume that a steady-state velocity field is achieved at the instant the angular velocity of the rotating fixture is changed. The steady-state velocity fields for parallel-plate and cone–plate flows have a (nearly) linear dependence on position in the gradient direction—the z-direction (parallel-plate), or the $\theta(\xi)$-direction (cone–plate). Hence, the shear rate is (nearly) uniform in the gradient direction for these flows. In the vorticity r-direction, the shear rate is a linear function of r for parallel-plate flow and is independent of r for cone–plate flow. Since the local stress depends on the local shear rate, the steady-state stress in the fluid is (nearly) uniform for cone–plate flow and is a linear function of r for parallel-plate flow. A major advantage of the rheologically controlled nature of parallel-plate and cone–plate flows is that these features of the steady-state velocity field are not dependent on the rheological behavior of the fluid.

Our analysis shows, however, that the time-dependent velocity fields for Newtonian fluids in parallel-plate and cone–plate flows are more complicated than those at steady state. Non-Newtonian fluids can have relatively large viscosities so that the time required for the velocity field to reach the steady state could be quite small. However rapidly this may occur, the velocity field of a non-Newtonian fluid for transient parallel-plate, or cone–plate, flow must evolve in time before reaching a steady state. Even though the results presented here are for Newtonian fluids, it is worthwhile to discuss the implications they may have on the rheometry of non-Newtonian fluids.

In general, the local state of stress in non-Newtonian fluids is a non-linear and time-dependent function of the local strain rate history. A commonly used measure of the strain rate is the second invariant of the rate of strain tensor: $\mathrm{II}_{\dot\gamma} = \sqrt{(\dot{\boldsymbol\gamma} : \dot{\boldsymbol\gamma})/2}$. For time-dependent parallel-plate flow with (59), $\mathrm{II}_{\dot\gamma}$ takes the form

$$\mathrm{II}_{\dot\gamma} = \frac{\partial v_\theta}{\partial z}, \tag{65}$$

which, at steady state, becomes $\mathrm{II}_{\dot\gamma} = r$. For cone–plate flow with (60), we have

$$\mathrm{II}_{\dot\gamma} = \sqrt{\left[r\frac{\partial}{\partial r}\left(\frac{v_\phi}{r}\right)\right]^2 + \left[\frac{1-\xi^2}{r}\frac{\partial}{\partial \xi}\left(\frac{v_\phi}{\sqrt{1-\xi^2}}\right)\right]^2}, \tag{66}$$

which reflects the three-dimensional nature of the time-dependent flow. At steady state, the velocity is linear in r so that $\mathrm{II}_{\dot\gamma} = 2|\gamma|/(1-\xi^2) \approx 1/\beta$ since $\xi \ll 1$. We note that, for parallel-plate flow, the dimensionless strain rate is of order one because the use of the parameter α ensures that both radial and axial positions are of order one. For cone–plate flow, the parameter β appears only in the boundary condition so that the azimuthal position $\xi \approx \beta$ for $\beta \ll 1$ is not of order one. For this reason, we normalize $\mathrm{II}_{\dot\gamma}$ with β for cone–plate flow.

Figure 13 shows the time evolution of $\mathrm{II}_{\dot\gamma}$ for parallel-plate flow. From this figure, we see for $\nu t/R^2 = 0.0003$ that the rate of strain tensor is highly non-homogeneous with variations in both the axial and radial directions. At the stationary disk ($z = 0$), $\mathrm{II}_{\dot\gamma}$ is approximately

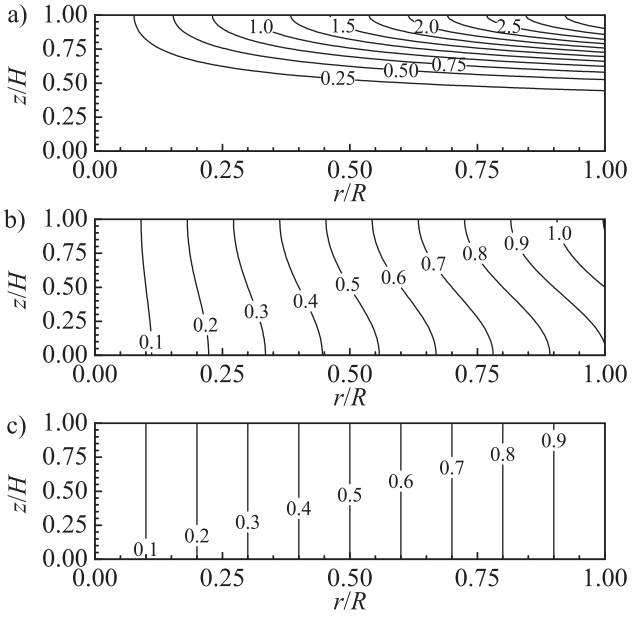

FIG. 13. Contour plots of the second invariant of the rate of strain tensor $\mathrm{II}_{\dot\gamma}$ for parallel-plate flow with $\alpha = 0.1$ for different times $\nu t/R^2$: (a) 0.0003; (b) 0.003; (c) 0.03.

zero, and at the edge of the rotating disk ($z = H$, $r = R$), the strain rate is more than a factor of three larger than the steady-state value. For $\nu t/R^2 \gtrsim 0.03$, the strain rate is nearly uniform in the gradient z-direction and has a linear dependence on r. The time evolution of $\beta \mathrm{II}_{\dot\gamma}$ for cone–plate flow is shown in Fig. 14. As with parallel-plate flow, for $\nu t/R^2 = 0.0003$, the rate of strain tensor is highly inhomogeneous, being approximately zero at the outer portion of the plate ($\xi = 0$, $r = R$) and more than three times larger than the steady-state value at the outer surface of the cone ($\xi = \xi_0$, $r = R$). However, for $r/R \lesssim 0.25$, the rate of strain is nearly uniform and approximately equal to the nominal steady-state value. The size of the nearly homogeneous region increases with increasing time. For $\nu t/R^2 \gtrsim 0.03$, the strain rate is uniform in the vorticity r-direction and varies by less than one percent in the gradient ξ-direction. One would expect that the rate of strain tensor would also be highly non-homogeneous for purely viscous non-Newtonian (e.g., power-law) fluids during the transient stage of parallel-plate or cone–plate flow.

It is of interest to note that cone–plate flows are commonly used to examine the effects of shear stress on endothelial cells and their biological functions.[29–31] Typically, the stationary plate is coated with cells, and the gap between the cone and the plate is filled with an aqueous (Newtonian) liquid. It is generally assumed that shear stress is uniform across the plate and that is known from the imposed shear rate and liquid viscosity. The results in Fig. 14 show that, at small times, the cells near the center of the plate would be subjected to the nominally applied shear stress, while cells near the edge of the plate would experience a much smaller shear stress.

We now consider the question of whether our results are related to the phenomenon known as *shear banding*. Shear banding, which is an instability that leads to the formation of fluid regions (bands) having different shear rates, has been the subject of intense research for the past several decades.[32–35] This phenomenon is observed for a wide range of complex (non-Newtonian) fluids that include worm-like micelles, polymer solutions, melts and gels, suspensions, emulsions, and foams. Observations of shear banding have been made using mechanical and optical rheological techniques that often are performed in parallel-plate or cone–plate geometries.[36]

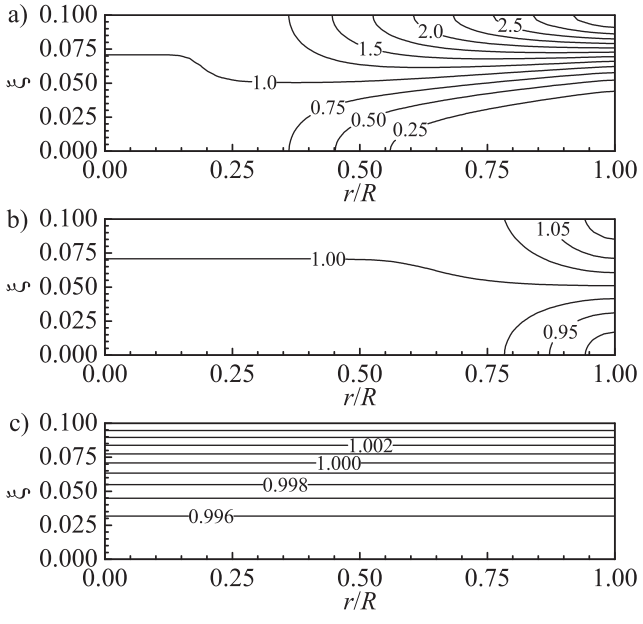

FIG. 14. Contour plots of the second invariant of the rate of strain tensor $\beta \mathrm{II}_{\dot\gamma}$ for cone–plate flow with $\beta = 0.1$ for different times $\nu t/R^2$: (a) 0.0003, (b) 0.003, and (c) 0.03.

Several explanations for shear banding have been proposed from levels of description ranging from mesoscopic to molecular.[37–41] A key ingredient in the proposed mechanism is the existence of a non-monotonic dependence of the steady-state shear stress on the shear rate. For fluids exhibiting this behavior, a given shear stress can be achieved at multiple shear rates. If a fluid is subjected to a shear rate within the range where the shear stress decreases with the increasing shear rate, shear bands having distinct shear rates can form. In such cases, the shear stress is (nearly) uniform in the gradient direction as required by the steady-state momentum balance. Measurements of the steady-state shear stress as a function of the shear rate are commonly made using parallel-plate and cone–plate rheometry. This, of course, is complicated by the fact that shear banding may be present in such measurements. However, other mechanisms that do not require a non-monotonic dependence of the steady-state shear stress on the shear rate have been proposed.[40,41] At present, it appears that the mechanism(s) responsible for shear banding has(have) yet to be definitively established.

We have just shown in Figs. 13 and 14 that the rate of strain is non-homogeneous during the transient stage of parallel-plate and cone–plate flows of Newtonian fluids. Here, we suggest that this inhomogeneity may be related to the formation of shear bands in complex fluids. Indeed, variations of $\mathrm{II}_{\dot\gamma}$ in the gradient direction can easily be a factor of 10 at small times following the imposition of a "constant" shear rate flow. The rheological behaviors of Newtonian and non-Newtonian fluids are, of course, qualitatively different, so our suggestion is purely speculative. Even for purely viscous non-Newtonian fluids, the momentum balance for both parallel-plate and cone–plate flows would be nonlinear and solvable only by numerical methods. We also recognize that the viscosity of complex fluids can be quite large so that the timescale for momentum diffusion could be quite small. Nevertheless, we believe that exploration of the time dependence of parallel-plate and cone–plate flows for complex fluids may be worthwhile in future efforts to understand shear banding phenomena.

IV. SUMMARY AND CONCLUSIONS

The dynamics of the velocity fields in parallel-plate and cone–plate flows are ignored in the analysis of rheological measurements employing these widely used geometries. Instead, a steady-state velocity field is assumed to exist throughout the measurement. In this study, we have investigated the dynamics of the velocity fields for parallel-plate and cone–plate flows of Newtonian fluids. Our results are based on heretofore unavailable analytical solutions of the Navier–Stokes equation in the creeping flow limit. The time-dependent solution for parallel-plate flow is relatively simple as it requires the velocity to have a linear dependence on radial position, which is the case for the steady-state solution. Somewhat surprisingly, the time-dependent velocity field for cone–plate flow does not have a linear dependence on radial position, which it must have at the steady state. As a result, it is three-dimensional and involves momentum diffusion in both the gradient and vorticity directions. The time-dependent velocity fields for these two flows are used to compute the time dependence of the

torque exerted on both the stationary and rotating fixtures. The time to reach a steady-state torque has a quadratic dependence on plate separation or cone angle. We find spatial inhomogeneities in the strain rate in both the gradient and vorticity directions, for both parallel-plate and cone–plate flows. While purely speculative, we suggest that the inhomogeneous strain rate within the fluid during the flow transient may be related to the shear banding phenomena observed in parallel-plate and cone–plate flows of complex fluids.

APPENDIX: EVALUATION OF THE SOLUTION FOR CONE–PLATE FLOW

The series solution for the cone–plate velocity field in (58) is computed in MATLAB. The coefficients A_{kn} in (55) involve integrals, which are computed using a built-in Gauss–Kronrod quadrature routine. The associated Legendre function of the first kind $P^1_\mu(\xi)$ is computed using the formula[42]

$$P^1_\mu(x) = -(\mu+1)\mu\left(\frac{1-x}{1+x}\right)^{1/2} F\left(\mu+1, -\mu; 2; \frac{1-x}{2}\right), \quad \text{(A1)}$$

where F is the hypergeometric function. The associated Legendre function of the second kind $Q^1_\mu(\xi)$ is computed using the formula[43]

$$Q^1_\mu(x) = -\frac{\pi}{2}\left[w_1(\mu,x)\cos\frac{\mu\pi}{2} + w_2(\mu,x)\sin\frac{\mu\pi}{2}\right], \quad \text{(A2)}$$

where

$$w_1(\mu,x) = \frac{2\Gamma\left(\frac{\mu}{2}+1\right)}{\Gamma\left(\frac{\mu}{2}+\frac{1}{2}\right)}(1-x^2)^{-1/2}\frac{F\left(-\frac{\mu}{2}-\frac{1}{2}, \frac{\mu}{2}; \frac{1}{2}; x^2\right)}{\Gamma(1/2)},$$
$$w_2(\mu,x) = \frac{2\Gamma\left(\frac{\mu}{2}+\frac{3}{2}\right)}{\Gamma\left(\frac{\mu}{2}\right)}x(1-x^2)^{-1/2}\frac{F\left(-\frac{\mu}{2}, \frac{\mu}{2}+\frac{1}{2}; \frac{3}{2}; x^2\right)}{\Gamma(3/2)}, \quad \text{(A3)}$$

and Γ is the gamma function. For large values of μ, numerical evaluation of the ratio of gamma functions in (A3) is unstable. We, thus, make use of the identity[44]

$$\frac{1}{z}\left(\frac{\Gamma(z+1)}{\Gamma(z+1/2)}\right)^2 = F\left(-\frac{1}{2}, -\frac{1}{2}; z; 1\right). \quad \text{(A4)}$$

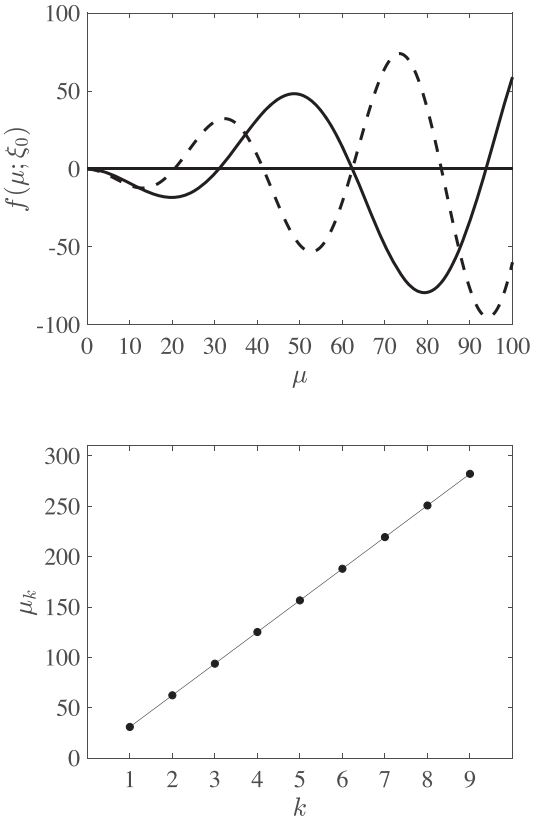

FIG. 15. Top panel: Plots of the function $f(\mu;\xi_0)$ defined in (44), for $\beta = 0.1$ (solid) and $\beta = 0.15$ (dashed). Bottom panel: Positive roots of f correspond to the eigenvalues $\{\mu_k\}_{k=1}^{\infty}$, the first nine of which are shown for $\beta = 0.1$.

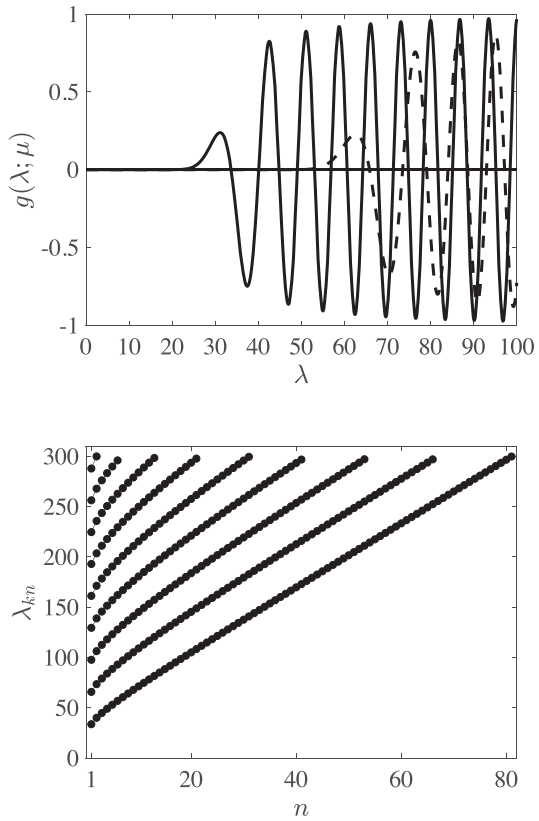

FIG. 16. Top panel: Plots of the function $g(\lambda;\mu)$ defined in (47) for $\mu = \mu_1 = 30.92$ (solid) and $\mu = \mu_2 = 62.33$ (dashed), which are the first two positive roots of $f(\mu;\xi_0)$ for $\beta = 0.1$ (see the bottom panel of Fig. 15). Bottom panel: Positive roots of $g(\lambda;\mu_k)$ correspond to the eigenvalues $\{\lambda_{kn}\}_{n=1}^{\infty}$. The curves are ordered by increasing values of k, the bottom being $k = 1$ and the top being $k = 9$.

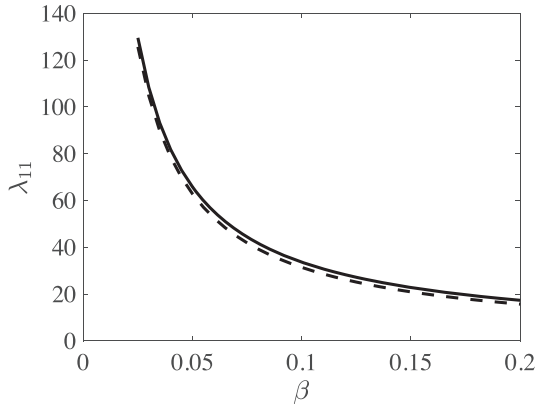

FIG. 17. The solid line shows the dependence of the smallest eigenvalue λ_{11} on the cone angle β. The dashed line indicates the approximation $\lambda_{11} \approx \pi/\beta$.

It follows that

$$\frac{\Gamma\left(\frac{\mu}{2}+1\right)}{\Gamma\left(\frac{\mu}{2}+\frac{1}{2}\right)} = \left[\frac{\mu}{2}F\left(-\frac{1}{2},-\frac{1}{2};\frac{\mu}{2};1\right)\right]^{1/2} \tag{A5}$$

and

$$\frac{\Gamma\left(\frac{\mu}{2}+\frac{3}{2}\right)}{\Gamma\left(\frac{\mu}{2}\right)} = \frac{\frac{\mu}{2}\left(\frac{\mu}{2}+\frac{1}{2}\right)\Gamma\left(\frac{\mu}{2}+\frac{1}{2}\right)}{\Gamma\left(\frac{\mu}{2}+1\right)} = \left(\frac{\mu}{2}+\frac{1}{2}\right)\left[\frac{\mu/2}{F\left(-\frac{1}{2},-\frac{1}{2};\frac{\mu}{2};1\right)}\right]^{1/2}, \tag{A6}$$

where, in (A6), we use the identity $\Gamma(z+1) = z\Gamma(z)$.

The eigenvalues μ_k (Fig. 15) and λ_{kn} (Fig. 16) are computed using bisection as the roots of $f(\mu;\xi_0)$ in (44) and $g(\lambda;\mu_k)$ in (47), respectively. We restrict our attention to $\lambda_{kn} \le \lambda_{\max} \equiv 300$ (Fig. 16, bottom panel) and truncate the infinite sum in (58) appropriately. For the smallest value of time $\nu t/R^2 = 3 \times 10^{-4}$ considered, we have $\exp\left(-\lambda_{\max}^2 \nu t/R^2\right) \sim 10^{-12}$, indicating that the solution in (58) is computed to high accuracy.

To evaluate M in (64) and $\Pi_{\dot\gamma}$ in (66), we make use of the formulas[26]

$$\frac{dP^1_{\mu_k}}{d\xi} = \frac{(\mu_k+1)P^1_{\mu_k-1} - (\mu_k-1)\xi P^1_{\mu_k}}{1-\xi^2}, \qquad \frac{dQ^1_{\mu_k}}{d\xi} = \frac{(\mu_k+1)Q^1_{\mu_k-1} - (\mu_k-1)\xi Q^1_{\mu_k}}{1-\xi^2}. \tag{A7}$$

DATA AVAILABILITY

The data that support the findings of this study are available from the corresponding author upon reasonable request.

REFERENCES

[1]K. Walters, *Rheometry* (Wiley, New York, 1975).
[2]C. W. Macosko, *Rheology: Principles, Measurements and Applications* (VCH Publishers, New York, 1994).
[3]R. B. Bird, R. C. Armstrong, and O. Hassager, *Dynamics of Polymeric Liquids*, 2nd ed., Fluid Mechanics Vol. 1 (Wiley, New York, 1987).
[4]N. Adams and A. S. Lodge, "Rheological properties of concentrated polymer solutions II. A cone-and-plate and parallel-plate pressure distribution apparatus for determining normal stress differences in steady shear flow," Philos. Trans. R. Soc. London Ser. A **256**, 149–184 (1964).
[5]A. J. Giacomin and P. H. Gilbert, "Exact-solution for cone-plate viscometry," J. Appl. Phys. **122**, 175101 (2017).
[6]J. C. Slattery, "Analysis of the cone-plate viscometer," J. Colloid Sci. **16**, 431–437 (1961).
[7]D. H. McCoy and M. M. Denn, "Secondary flow in a parallel-disk viscometer," Rheol. Acta **10**, 408–411 (1971).
[8]R. M. Turian, "Perturbation solution of the steady Newtonian flow in the cone and plate and parallel plate systems," Ind. Eng. Chem. Fundam. **11**, 361–368 (1972).
[9]M. E. Fewell and J. D. Hellums, "The secondary flow of Newtonian fluids in cone-and-plate viscometers," Trans. Soc. Rheol. **21**, 535–565 (1977).
[10]G. H. McKinley, J. A. Byars, R. A. Brown, and R. C. Armstrong, "Observations on the elastic instability in cone-and-plate and parallel-plate flows of a polyisobutylene Boger fluid," J. Non-Newtonian Fluid Mech. **40**, 201–229 (1991).
[11]D. F. Griffiths and K. Walters, "On edge effects in rheometry," J. Fluid Mech. **42**, 379–399 (1970).
[12]D. O. Olagunju, "Effect of free surface and inertia on viscoelastic parallel plate flow," J. Rheol. **38**, 151–168 (1994).
[13]J. S. Vrentas, D. C. Venerus, and C. M. Vrentas, "An exact analysis of reservoir effects for rotational viscometers," Chem. Eng. Sci. **46**, 33–37 (1991).
[14]D. C. Venerus, "Free surface effects on normal stress measurements in cone and plate flow," Appl. Rheol. **17**, 36494 (2007).
[15]A. Yoshimura and R. K. Prud'homme, "Wall slip corrections for Couette and parallel disk viscometers," J. Rheol. **32**, 53–67 (1988).
[16]R. B. Bird and R. M. Turian, "Viscous heating effects in a cone and plate viscometer," Chem. Eng. Sci. **17**, 331–334 (1962).
[17]D. O. Olagunju, A. B. Vyas, and S. Zhang, "Analytical and numerical solutions for torsional flow between coaxial discs with heat transfer," SIAM J. Appl. Math. **68**, 1404–1422 (2008).
[18]M. G. Hansen and F. Nazem, "Transient normal force transducer response in a modified Weissenberg rheogoniometer," J. Rheol. **19**, 21–36 (1975).
[19]T. Schweizer and A. Bardow, "The role of instrument compliance in normal force measurements of polymer melts," Rheol. Acta **45**, 393–402 (2006).
[20]C. S. Dutcher and D. C. Venerus, "Compliance effects on the torsional flow of a viscoelastic fluid," J. Non-Newtonian Fluid Mech. **150**, 154–161 (2008).
[21]R. B. Bird and C. F. Curtiss, "Tangential Newtonian flow in annuli-I: Unsteady state velocity profiles," Chem. Eng. Sci. **11**, 108–113 (1959).
[22]J. Passard, R. Kouitat Njiwa, and P. Perré, "Unsteady flow in cone and plate geometry: How computation can help rheometry," Eur. Phys. J.: Appl. Phys. **3**, 321–342 (1998).
[23]D. C. Venerus and H. C. Öttinger, *A Modern Course in Transport Phenomena* (Cambridge University Press, Cambridge, 2018).
[24]H. S. Carslaw and J. C. Jaeger, *Conduction of Heat in Solids*, 2nd ed. (Oxford University Press, New York, 1959).
[25]J. C. Slattery, *Advanced Transport Phenomena*, Cambridge Series in Chemical Engineering (Cambridge University Press, New York, 1999).
[26]E. W. Hobson, *The Theory of Spherical and Ellipsoidal Harmonics* (Cambridge University Press, Cambridge, 1931).
[27]M. Abramowitz and E. I. A. Stegun, *Handbook of Mathematical Functions with Formulas, Graphs, and Mathematical Tables* (Dover, New York, 1965).

[28]These functions are related to the usual Bessel functions by the formulas $j_n(z) = \sqrt{\frac{\pi}{2z}}J_{n+1/2}(z)$ and $y_n(z) = \sqrt{\frac{\pi}{2z}}Y_{n+1/2}(z)$.

[29]C. F. Dewey, S. R. Bussolari, M. A. Gimbrone, and P. F. Davies, "The dynamic response of vascular endothelial cells to fluid shear stress," J. Biomech. Eng. **103**, 177–185 (1981).
[30]T. Nagel, N. Resnick, C. F. Dewey, and M. A. Gimbrone, "Vascular endothelial cells respond to spatial gradients in fluid shear stress by enhanced activation of transcription factors," Arterioscler., Thromb., Vasc. Biol. **19**, 1825–1834 (1999).
[31]M. H. Buschmann, P. Dieterich, N. A. Adams, and H.-J. Schnittler, "Analysis of flow in a cone-and-plate apparatus with respect to spatial and temporal effects on endothelial cells," Biotech. Bioeng. **89**, 493–502 (2005).
[32]P. Tapadia and S.-Q. Wang, "Direct visualization of continuous simple shear in non-Newtonian polymeric fluids," Phys. Rev. Lett. **96**, 016001 (2006).
[33]S. Ravindranath, S.-Q. Wang, M. Olechnowicz, and R. P. Quirk, "Banding in simple steady shear of entangled polymer solutions," Macromolecules **41**, 2663–2670 (2008).
[34]P. D. Olmsted, "Perspectives on shear banding in complex fluids," Rheol. Acta **47**, 283–300 (2008).
[35]G. Ovarlez, S. Rodts, X. Chateau, and P. Coussot, "Phenomenology and physical origin of shear localization and shear banding in complex fluids," Rheol. Acta **48**, 831–844 (2009).
[36]Y. Li, M. Hu, G. B. McKenna, C. J. Dimitriou, G. H. McKinley, R. M. Mick, D. C. Venerus, and L. A. Archer, "Flow field visualization of entangled polybutadiene solutions under nonlinear viscoelastic flow conditions," J. Rheol. **57**, 1411 (2013).
[37]R. L. Moorcroft and S. M. Fielding, "Criteria for shear banding in time-dependent flows of complex fluids," Phys. Rev. Lett. **110**, 086001 (2013).
[38]M. Mohagheghi and B. Khomami, "Elucidating the flow-microstructure coupling in entangled polymer melts. Part II: Molecular mechanism of shear banding," J. Rheol. **60**, 861–872 (2016).
[39]T. Divoux, M. A. Fardin, S. Manneville, and S. Lerouge, "Shear banding of complex fluids," Annu. Rev. Fluid Mech. **48**, 81–103 (2016).
[40]E. J. Hemingway and S. M. Fielding, "Interplay of edge fracture and shear banding in complex fluids," J. Rheol. **64**, 1147–1159 (2020).
[41]M. Boudaghi-Khajehnobar, B. J. Edwards, and B. Khomami, "Effects of chain length and polydispersity on shear banding in simple shear flow of polymeric melts," Soft Matter **16**, 6468–6483 (2020).
[42]See https://dlmf.nist.gov/14.3#E5 for a formula for the associated Legendre function of the first kind.
[43]See https://dlmf.nist.gov/14.3#E12 for a formula for the associated Legendre function of the second kind.
[44]G. N. Watson, "A note on gamma functions," Proc. Edinburgh Math. Soc. **42**, 7–9 (1959).